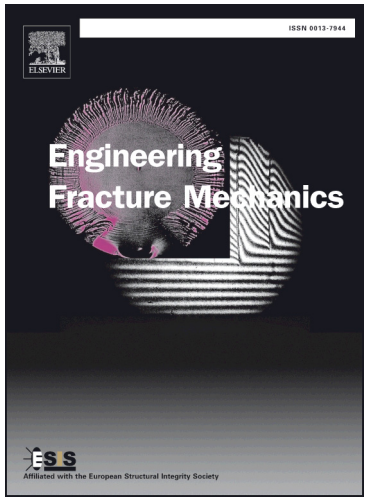

A Study of Overload Effect on Fatigue Crack Propagation Using EBSD, FIB-DIC and FEM Methods

E. Salvati, S. O'Connor, T. Sui, D. Nowell, A.M. Korsunsky

PII: S0013-7944(16)30199-0
DOI: http://dx.doi.org/10.1016/j.engfracmech.2016.04.034
Reference: EFM 5179

To appear in: *Engineering Fracture Mechanics*

Received Date: 2 December 2015
Revised Date: 6 April 2016
Accepted Date: 18 April 2016

Please cite this article as: Salvati, E., O'Connor, S., Sui, T., Nowell, D., Korsunsky, A.M., A Study of Overload Effect on Fatigue Crack Propagation Using EBSD, FIB-DIC and FEM Methods, *Engineering Fracture Mechanics* (2016), doi: http://dx.doi.org/10.1016/j.engfracmech.2016.04.034

A Study of Overload Effect on Fatigue Crack Propagation Using EBSD, FIB-DIC and FEM Methods

E. Salvati, S. O'Connor, T. Sui, D. Nowell, A.M. Korsunsky

Department of Engineering Science, University of Oxford, Parks Road, Oxford, OX13PJ, United Kingdom

Corresponding author:

Alexander M. Korsunsky

Department of Engineering Science
University of Oxford
Parks Road
Oxford OX1 3PJ
United Kingdom

Tel: +44-18652-73043

Fax: +44-18652-73010

E-Mail: alexander.korsunsky@eng.ox.ac.uk

Abstract

Abrupt increase in the maximum load during fatigue cycling modifies the deformation conditions at the crack tip, causing plastic flow that may lead to crack closure, introducing residual stress and hardening. The net consequence of these effects is notable crack growth retardation. Despite decades of research in the field, controversy persists regarding the role of each specific mechanism and their interaction. Resolving these issues with the help of experimental observation is related to the difficulty of obtaining local residual stress information at appropriate resolution. The present study examines the effect of overload on fatigue crack grown in a Compact Tension (CT) specimen of aluminium alloy AA6082 (BS HE30). Fatigue crack was grown in the sample under cyclic tension (R=0.1). After the application of a single overload cycle, fatigue loading was recommenced under previous cycling conditions. The crack morphology was investigated using Scanning Electron Microscopy (SEM). Electron Backscattered Diffraction (EBSD) was used to map grain orientation and crystal lattice distortion (pattern quality) in the vicinity of the crack. EBSD analysis of intra-granular misorientation allowed the qualitative analysis of the region around the crack tip location at the time of the overload application. Observations are discussed with a view to identify the roles of crack closure and residual stress effects. Residual stress was evaluated at salient locations around the crack retardation site using the FIB-DIC method which combines the use of Focused Ion Beam (FIB) and Digital Image Correlation (DIC) for residual stress measurement at the (sub)micron-scale. The residual stress field due to overload occurrence was also simulated using Finite Element Method (FEM), and the results compared with experimental observations.

1. Introduction

Variable amplitude fatigue is a common loading mode for mechanical components in service. To optimise the reliability of engineering components under variable amplitude, the crack growth rate needs to be quantified and fatigue life estimated. The fatigue crack growth rate (FCGR) is affected by the plastic deformation at the crack tip, caused by the remote load application. However, the correlation between the loading spectrum and the fatigue life is complex and may sometimes appear counter-intuitive. To elucidate the effect of external load variation on crack growth, the effects of an elementary occurrence of a single Overload (OL) or Underload (UL) are often examined [1-2]. Generally, underload (UL), i.e. the application of compressive load to the crack accelerates it, whilst overload (OL) leads to a retardation of the fatigue crack propagation. A quantitative measure of FCGR reduction due to the OL is the number of cycles that it takes for the crack to regain the original steady state growth rate. The retardation is related to all aspects of material structure and state change around the crack tip, and persists until the crack grows out of the region perturbed by the OL application. Immediately after the application of an OL, a very short acceleration of the propagation rate may be observed before the retardation sets in. This event appears especially when the OL ratio is greater than 1.5 ($R_{OL}=F_{OL}/F_{max}$) with respect to the cyclic load maximum is relatively high [2] and it is thought to be due the significant the damage induced by OL in the material surrounding the crack tip. The size of the plastic zone at the crack tip is one of the most important parameters that determines the conditions of its advancement. Further, variation in the specimen thickness changes the stress state within the sample and around the crack from being closer to plane stress or plane strain. Hence specimen thickness determines the overall apparent plastic zone size. Retardation or acceleration may depend not only on the UL or OL being applied, but also on the stress ratio. In fact, it has been shown [3] that in some cases a negative stress ratio in combination with an OL may cause acceleration of fatigue crack growth instead of the expected

retardation. Furthermore, it has been shown that under negative load ratio the cyclic plastic properties of the material play an important role in determining the crack propagation rate.

The effect of retardation can be attributed to several mechanisms. In most cases an OL leads to crack blunting. Hence further crack propagation may require crack re-nucleation, with a consequent delay in crack growth.

Another mechanism, perhaps the most important to mention in the context of crack retardation, is the crack closure effect [5]. An OL causes plastic deformation at the crack tip, and produces excess material just ahead of it. Once the crack tip moves beyond this region, the crack flanks maintain contact causing the crack tip to be delayed, reducing the effective stress intensity factor range ΔK, and with it the crack growth rate.

Another often used explanation for crack retardation is the presence of residual stress at the crack tip [6-7]. The large plastic deformation at the crack tip induced by the OL generates compressive residual stress that induces crack retardation associated with either re-nucleation or slower propagation. At micro-scale the behaviour of small material volumes may be anisotropic, contributing to the variation in response between samples and locations [8]. The residual stress effect can be accounted for in terms of the additional Stress Intensity Factor terms acting locally at the crack tip [9]. The effect of crack tip shielding induced by plastic deformation can also be taken into account during fatigue endurance evaluation by means of the modified SIF or Weight Function method, as proposed in [10].

The knowledge of the local behaviour of the material at the vicinity of the crack tip therefore plays a crucial role in the problem of crack propagation and retardation. Hence, the evaluation of the stress-strain state that arises in the process zone is necessary. However, the small size of the plastic zone for materials of interest means that few techniques are available for the task. One such technique is micro-indentation [11] which can map mechanical properties at good special resolution, but is unable to deliver sufficient accuracy for residual stress evaluation. It has been reported [6,8,9] that, the use of synchrotron X-ray diffraction, allowed high-resolution mapping of the region of interest,

including under in situ loading. An important advantage of the method being that it is truly non-destructive and non-invasive.

Electron BackScattered Diffraction (EBSD) technique is steadily gaining popularity as a tool used for material characterization at the micro- and nano-scale. The capability of determining grain orientation in polycrystalline materials is the reason for EBSD also finding use for the examination of crack propagation conditions [12-13]. It may help to reveal the dependence of crack propagation on grain misorientation and grain boundary effects. The local distortion of the crystal lattice within a single grain can be captured by EBSD through careful analysis of Kikuchi pattern deformation, allowing both the misorientation angle(s) and lattice strains to be extracted [14]. The quality of a Kikuchi pattern is sensitive to the severity of lattice distortion within the sample's volume, and can thus provide useful information about the amount of plastic deformation experienced by the elementary material volume, and hence is related to the origins of residual stress. The numerical quantification of the strain present in the material can be performed using the so-called High Resolution EBSD (HR-EBSD) [15-16]. This technique is based on the analysis of Kikuchi pattern shifts and rotations which can be related to the magnitude and nature of the lattice strain variation. Of course, like all the methods using diffraction (e.g. X-ray Diffraction), the reference state of the material for a given grain orientation has to be known a priori, i.e. a strain-free location or a reference pattern. Alternatively, without the knowledge of such information, it is possible to reconstruct a qualitative residual stress map over the scanned area to provide some insights into stress variation for the areas where the strains are relatively high. The method has limitations in terms of strain precision, and is likely to fail for regions of significant plastic deformation [16]. It is also very sensitive to the quality of sample surface preparation, since plastic deformation that arises as a consequence of the polishing procedure may remain in the sample.

Another promising method for the experimental quantification of stresses at micron scale is FIB-DIC micro-ring core drilling [17-18]. If new traction-free surfaces are created in the vicinity of a particular material volume, quantification of deformation at the sample surface and evaluation of strain relief

furnishes information about the pre-existing residual stress state. The version of the technique advanced in the MBLEM lab at Oxford is based on the use of Focused Ion Beam (FIB) as the means of minimally invasive [19] creation of a circular traction-free trench around the central micro-pillar. The deformation occurring at the pillar top surface is monitored during milling using SEM, and interpreted using Digital Image Correlation (DIC). The mean strain relief at the pillar surface can be directly correlated to the magnitude and nature of the residual stress state present in the material prior to milling using a fitting function calibrated by Finite Element Analysis [20]. One of the advantages of this technique is its universal applicability to non-crystalline, heavily deformed, inhomogeneous, fine and coarse grained materials alike, for which other techniques based on diffraction (XRD, HR-EBSD) fail; together with the obviation of the need for a reference strain-free sample.

The aluminium alloy Compact Tension Specimen that was the subject of the present study was first cycled at a constant load amplitude and load ratio R=0.1 to induce crack nucleation and propagation. An overload (OL) was then applied at a certain crack length. After this, the original constant amplitude cyclic loading was continued until the fatigue crack growth rate (FCGR) prior to the OL was recovered. The evolution of the crack at the surface of the specimen was monitored by microscopic imaging using in-situ loading in a Scanning Electron Microscope (SEM). The crack surfaces were also examined afterwards using the same SEM. The crack path, morphology, microstructure and residual stress around a crack propagated beyond an OL was examined. EBSD was used to map the region of interest around the crack to help in understanding the microstructural mechanisms involved in the crack retardation induced by the OL. By analysing the intragranular misorientation it was possible to obtain an indication of the plastic strain distribution in the vicinity of the crack flanks and near the tip. Experimental quantification of residual stress was performed at chosen salient locations using the FIB-DIC ring-core method. Experimental residual stress results were assessed and interpreted by means of comparison with Finite Element Modelling (FEM) of near crack-tip plastic strain at the OL

location and at the final crack tip. This comparison allowed the understanding of which characteristics of crack propagation can be captured using a fundamental model. Especially at this small scale where microstructural features may play their relevant role and therefore a more complex model would be required.

2. Fatigue test

2.1 Experimental Procedure

The sample used to carry out this experiment was made from aluminium alloy AA6082 (BS specification HE30). A 35mm miniature Compact Tension (CT) sample was machined from a 3mm thick rolled plate. Figure 1a depicts the geometric shape, the characteristic dimensions and the direction of the applied load. In this experiment, a relatively sharp fillet radius was created at the notch tip (R<0.1mm) to facilitate pre-cracking. Fatigue testing was conducted using a servo-hydraulic machine, for the crack nucleation and first propagation segment, and in a compact *in situ* tensile testing stage was used in an SEM for the overload application and further propagation. The loading history is schematically described in Figure 1b.

<Figure 1 here>

For the first step, from the point A to B' (Fig. 1b) the applied force range was $\Delta F=1.125kN$, the maximum cyclic load $F_{max}=1.25kN$ and the minimum $F_{min}=0.125kN$. After 17000 cycles the crack had propagated to a total length, a, of 7mm. Cyclic loading was then interrupted and several SEM images were taken along the entire crack extension. At this stage (Point OL in Fig. 1b), the specimen was subjected to a single 50% overload of magnitude $F_{OL}=1.875kN$ ($1.5 \cdot F_{max}$). The same constant amplitude test used previously was then conducted for a further 1000 cycles. At the end of the fatigue test the crack had grown a further 0.4mm in length (point D' in Fig. 2b). The crack was imaged at various locations, with particular attention to the extent of crack associated with its

growth past the point of overload application. This procedure allowed comparison to be made with the previous crack morphology prior to overload application.

The Stress Intensity Factor (SIF) can be evaluated for any crack length using the formula [21]:

$$K_I = \frac{F}{b}\sqrt{\frac{\pi}{W}}\left[16.7\left(\frac{a}{W}\right)^{\frac{1}{2}} - 104.7\left(\frac{a}{W}\right)^{\frac{3}{2}} + 369.9\left(\frac{a}{W}\right)^{\frac{5}{2}} - 573.8\left(\frac{a}{W}\right)^{\frac{7}{2}} + 360.5\left(\frac{a}{W}\right)^{\frac{9}{2}}\right] \quad (1)$$

Here *a* is the crack length from the point of load application, *W* is the total ligament width, and *b* denotes the specimen thickness. These dimensions are illustrated in Figure 1.At the first application of cyclic loading before crack propagation, the SIF range applied to the sample was ΔK_A*=11.87 MPa √m.* As the crack extended, the SIF increased and reached the value of ΔK_B*=19.45 MPa √m* at point B. The overload applied at that crack depth corresponded to the magnitude of SIF equal to K_{OL}*=32.42 MPa √m.* According to Irwin's formulation [22] for the plastic zone determination, such plastic zone turned out to be of 0.94mm. The test was continued and ultimately arrested at point D where the final SIF range was ΔK_D*=20.23 MPa √m.*

2.2 Crack growth behaviour

The fatigue crack growth rate (FCGR) is summarised in the Paris diagram shown in Fig. 2.

<Figure 2 here>

As expected, right after the overload application the crack propagation was retarded; d*a*/d*n* drops immediately by an order of magnitude, and only gradually returns to the steady state behaviour. Assuming that at the last point of measurement of crack length, the crack had reached the unaltered material zone, the FCGR curve can be described analytically according to Paris' Law with the coefficients *C* and *m* reported in Fig 2:

$$\frac{da}{dn} = C\ \Delta K^m \quad (2)$$

3. SEM and EBSD analysis

3.1. SEM imaging analysis

The application of an overload causes retardation of crack propagation that constitutes a considerable improvement in fatigue resistance of the mechanical component examined. In the present study we are focusing exclusively on the study of the mechanisms that operate during and following the OL, without considering the effective retardation of the crack propagation in terms of the number of cycles.

SEM imaging of the crack flanks prior (B in Fig.1b) and after the application of the overload (D' in Fig.1b) has allowed the visualization of the crack shape and its evolution due to and past the overload. The crack propagated through the material in the direction perpendicular to the predominant cyclic tensile stress. The crack image taken at point B in the propagation history is shown in Figure 3a. To collect this image, the sample was loaded to F_{max}*=1.25kN* and the surface imaged in the unpolished state. At this stage the crack flanks appear rough. Significant out-of-plane plastic deformation at crack flanks is not apparent. In contrast, the image of the crack taken at point D' in its propagation history (Fig.3b) shows the crack flanks being in contact over the entire length of crack between points B and D'. In the region of contact, some evidence of local out-of-plane plastic deformation can be found. Such deformation is the consequence of intense local compression that induced material flow and extrusion in the direction of least constraint (out-of-plane). These considerations suggest that crack propagation beyond the OL was accompanied by crack closure.

<Figure 3 here>

Focusing now on the crack tip at the time of overload application, the following observations and comments can be made. In Figure 4 the crack tip is shown at several points during the overload cycle (before OL at maximum force, and after OL at minimum force). The crack tip at B' is illustrated in Figure 4a. The OL ultimately led to additional crack extension of around 10μm, as seen from the comparison with Figure 4b. Following the OL, the crack propagation in this direction was halted, and fracture continued to grow in a direction different from the previous growth direction at the tip. Moreover, crack growth in Mode I appears to have been arrested.. There is also evidence of significant crack tip blunting. The crack remained stationary until a new nucleation direction was established (Figure 4d). It is worth noting that this new propagation direction lies at approximately 90˚ to the original crack growth direction, and possesses significant Mode II character. The same crack deviation right after OL was experienced by several authors [23-25]. The crack therefore prefers to propagate around the plastic zone instead of advancing along its original path direction.

<Figure 4 here>

3.2 EBSD analysis

EBSD technique was adopted for the purpose of mapping the grain morphology and orientation around the crack. Crystal lattice orientation varies both between and within grains (intragranular misorientation). The latter in particular is closely associated with plastic deformation and strain gradients induced by dislocation glide. Note that whilst statistically stored dislocations (SSD) accommodate uniform plastic strain causing significant lattice distortion by little rotation, geometrically necessary dislocations (GND) that accommodate steep changes in plastic strain (such as observed at crack tips) lead to large lattice rotation and hence misorientation [26-27]. Therefore, capturing misorientation variation is of interest for the purpose of characterising intragranular

deformation gradients, e.g. from features such as slip bands or dislocation pile-ups in the vicinity of grain boundaries. EBSD analysis requires a well-polished sample surface. To obtain extremely smooth, good quality surface the sample was reduced in size to contain only the region of interest and ground with abrasive cloths up to 1200 grade. Then, smooth cloth polishing with 3µm and 1µm diamond suspension was adopted. The final polishing step used 0.1 µm colloidal silica, with subsequent addition of hydrogen peroxide to reduce potential deposits.

The sample was mapped using an electron beam at 25kV energy and 18.5nA current. Two main acquisition steps were performed. The first was an overview of the crack that comprises the location that the crack passed before the application of the overload; the pixel size in this last case was 3.2µm. The second mapping stage focused on imaging the region of overload application and subsequent propagation with the pixel size of 0.76µm.The grain shape and boundaries can be visualized in detail by means of EBSD analysis. Since considerable amount of material was removed during surface preparation, the crack morphology appears slightly different in Fig.5 and Fig.7 from that previously seen in Fig.3 and Fig.4.

The EBSD map in Figure 5 shows that morphologically the grains have a somewhat elongated shape in the rolling direction, and the grain size varies between 20-250µm. In Figure 6 the pole figure is reported for the three main phases used for Kikuchi pattern indexing, accounting for over 95% of the indexed points. These three phases were: Al (51.4%), $Al_{0.3}\,Cu_{7.01}\,Fe_{1.7}\,Mg_{0.2}$ (15.9%) and Al Mn_3 (27.7%). The pole figures reveal the preferred orientation of the crystals that is close to the <001> direction being aligned with the rolling direction defined in Fig.1. This orientation preference was confirmed for all three phases. The analysis of the crack propagation manner within the microstructure has highlighted a predominant transgranular mode (i.e. cutting grains). Quantitatively, transgranular propagation occurs for ~60% of the grain involved in the crack propagation and, in the remaining ~40%, the propagation is intergranular mode.

Except for few grains on left side of the Figure (Fig.5) where the propagation manner is unclear, the crack propagated mainly in a transgranular mode.

The coarse mapping of the cracked surface, overlaid on the band contrast map, (Fig.5) shows the crystal orientation of the grains surrounding the crack. As expected, orientation indexation presented a challenge at the crack line and in other regions where large plastic deformation occurred. The position of the large deformation caused by the overload is represented by the yellow circle shown in the Figure 5. At this position it was not possible to obtain grain orientation form Kikuchi pattern analysis, due to the large plastic strain causing severe distortion of the crystal lattice leading to the degradation in the pattern quality.

<Figure 5 here>

<Figure 6 here>

A more detailed analysis of the grain orientation is shown in Figure 7a. The purpose of this map is the collection of the EBSD information focusing more closely on the region of crack propagation after the overload. The high-resolution mapping mode (pixel size 0.76 μm) allowed the visualization not only of the grain orientation, but also the relative changes in orientation within a single grain, i.e. intragranular lattice misorientation [28]. Regarding the crack closure effect after the overload, the EBSD map provides the following insight. At the crack flanks the local orientation is highly affected by their contact. These changes in the local orientation are due to the plastic deformation in the direction perpendicular to the crack surface. This provides additional supporting evidence of the crack closure effect present during the propagation phase derived from EBSD analysis.

The misorientation observed within grains provides indirect information about the strain distribution within the material. The interpretation of misorientation using the grain-based approach [14] allowed the graphic representation of the regions affected by high strain. The result is shown in

Figure 7b that shows the map acquired at zero load and is related to residual plastic strain. The map is qualitative, so that no colour bar is provided, but the conventional “reduced rainbow” colour scheme is used, with blue corresponding to low and red to high values. The regions of high residual plastic strain are located in the vicinity of the crack line, as expected. The residual strain that arises along the crack flank is associated with the process zone at the crack tip during propagation. Another potential cause may be the plastic deformation due to crack surface contact as described previously. The region associated with the OL is indicated by the letter “A” in Figure 7. No evident alteration was experienced in this area. Especially at the very vicinity of the crack flank, where the lattice distortion is particularly high and, as a consequence, indexation of the backscattered pattern was not possible, and the orientation map could not be acquired for the totality of the scanned pixels. However, the lack of indexing is itself an indication of the plastic deformation occurred. For this reason, we can consider the region near the OL location one of the most stressed regions.

In any case, according to the plastic region extension evaluated through Irwin’s formulation (0.94mm), the entire region mapped by EBSD lies in the plastic zone. This may justify the graphical absence of the expected high plastic deformation surrounding the OL site. Furthermore, since such technique is mainly able to capture plastic deformation change within grains [29], we cannot rely on the comparison between the plastically deformed regions at different grains.

The presence of the region of high residual plastic strain expected at the crack tip is confirmed (indicated by the letter “B” in Fig.7).

<Figure 7 here>

4. Residual Stress measurement and numerical interpretation

4.1 FIB-DIC ring-core measurements

Analysis conducted using EBSD mapping highlights the regions where significant plastic deformation occurred. For instance, at the OL site, the lack of indexation of the Kikuchi patterns indicated that localised large plastic deformation occurred. Nevertheless, since the entire map lies on the OL plastic zone, no evident differences in plastic deformation can be observed along the crack path except some very localised areas. In order to provide quantitative information about residual stresses, FIB-DIC ring-core measurements were conducted at carefully selected locations. It is worth noting that all measurements conducted corresponded to the last stage of crack propagation, i.e. point D'' indicated in Fig.1b. The locations of interest (sites) where we focused our effort are reported below and graphically represented in Fig.8

I) Several locations along the crack path at 15-30 μm from either the crack flank (dotted in Fig.9)
II) A line of measurements aligned perpendicular to the crack line 20 μm behind the OL site
III) A line of measurements aligned perpendicular to the crack line at the OL site
IV) A line of measurements perpendicular to the crack at the final crack tip
V) A line of measurement along the crack continuation ahead of the crack tip

Since the FIB-DIC method relies on the DIC analysis for the quantification of strain relief, the pillar top surface needs to show reasonable contrast so that the displacements can be evaluated accurately. Since the polished surface does not possess such inherent contrast, the sample surface was coated with an extremely thin (~5nm) soft layer of sputtered Au-Pd. Such coating layer provided a randomly distributed texture onto the surface ideal for DIC analysis, and at the same time does not introduce any additional stress to modify the pre-existing conditions.

At each measuring point, the incremental procedure of material removal was followed [17] that produced a sequence of n=50 images. An illustration of the milling process as the material is being removed and the images acquired is depicted in the figure below:

<Figure 8 here>

These images were analysed using DIC software [30] and a data refinement procedure was adopted for the detection and rejection of outliers. As a result, strain relief curves were obtained for two orthogonal directions associated with the crack growth direction that were labelled *x* and *y* as defined in Fig.9

<Figure 9 here>

The experimentally determined strain evolution can be described by a parametric function [31] developed on the basis of Finite Element Analysis (FEA). At the end of the fitting procedure, the residual strain and its standard deviation were evaluated at 95% confidence.

As the last step, the residual stress was evaluated using Hooke's law under the assumption of plane stress state:

$$\sigma_{xx} = \frac{E}{(1-\nu^2)}\left[\varepsilon_{xx} + \nu\,\varepsilon_{yy}\right] \tag{2}$$

$$\sigma_{yy} = \frac{E}{(1-\nu^2)}\left[\varepsilon_{yy} + \nu\,\varepsilon_{xx}\right] \tag{3}$$

The evaluation of residual stress at this small scale introduces a further source of error due the material elastic anisotropy within the single grain. Since the examined material shows large structured grains, there is a high probability that the milling point lies within a single grain and therefore, the elastic anisotropy may affect the evaluated value of stress. Recent work [32] reported a statistical approach to quantifying this if the local grain orientation is unknown. According to this

paper, the error at 95% of confidence for aluminium alloy amounts to 8%. This was taken into account alongside other sources of error (i.e. DIC peak tracking and relief strain fitting procedure), and the overall uncertainty reported as error bands in the resulting plots.

4.2 Residual stress modelling

Since the purpose of the simulation was to make comparison with experimental measurements using FIB-DIC ring-core milling at sample surface, a two-dimensional plane stress modelling was employed. The software used for FEM simulation was Abaqus©. In the simulation described below the material was assumed to follow the isotropic hardening rule having hardening exponent n=0.05 and strength coefficient K=540MPa. Taking advantage of the specimen symmetry, half model was generated and meshed as shown in Fig.10. Mesh refinement was introduced at the locations corresponding to the locations of FIB-DIC line measurements. In order to achieve accurate simulation results, a convergence analysis was performed; the optimal mesh element size at the region of interest turned out to be of 2µm. The displacement boundary condition due to symmetry was applied at the nodes where no material separation was present. Crack advance was simulated by progressive removal of boundary conditions requiring the nodes to remain bonded. Crack flank interpenetration at locations where plasticity crack closure took place during the unloading phase was avoided using a fictitious contact surface opposing the crack flank. The inequality describing the contact condition was unilateral so that the crack was free to open. As described in a previous publication [33], this technique has been shown to be successful at simulating residual stress evolution at the crack tip. The model was progressively run at three different stages of crack propagation in order to attempt capturing the stress field evolution. The first stage considered a crack length of 35 µm shorter than the one at the OL, the second at the OL and the third at the last at the stage indicated as D'' in Fig.1b.

<Figure 10 here>

4.3. Results and discussion

In this section, residual stress predictions provided by FE modelling are compared with the evaluation by means of FIB-DIC ring-core milling. Within the model, residual stress quantification was performed for the situation when the crack has propagated past the locations on the crack flanks depicted by the dots in Fig.9. We begin the discussion with the analysis of experimental results for stresses along the crack that are shown in Fig.11. It shows the variation of the measured residual stress values along the crack line (markers and error bars). Continuous curves through the markers are given as a guide to the eye. The overload location corresponds to $x = 0$. It is apparent from the plot that behind the overload ($x < 0$), a slight compressive residual stress layer is present. Both stress components manifest a similar magnitude that lies in the range between -150MPa and -50MPa.

Leaving aside the overload location that will be examined in detail later, we note another region of moderate compressive residual stress found along the crack flanks at locations corresponding to crack growth past the overload. Particularly, at 0.48mm forward from the overload site, a more compressive value of residual stress was measured in the crack opening direction (*yy* component). It is worth noting that this location corresponds to the region of high plastic deformation highlighted by EBSD mapping and indicated by the square in Fig.7b.

<Figure 11 here>

The sites II, III, IV and V were numerically modelled; some contour images are reported below in Fig.12.

<Figure 12 here>

Below we report direct comparison between numerical and experimental results for selected lines indicated in Fig. 10. Line plots of stress components *xx* and *yy* are given in Fig. 13.

<Figure 13 here>

Focusing our attention on the region close to the overload location (Fig. 13a,b,c,d), the compressive residual stress field induced by this single anomalous load application is evident. Compressive stress values that reach -450MPa were measured. At Site II (Fig.13a-b) the *xx* stress component is well matched in magnitude. The trend of the *yy* stress component shows good agreement. However, the same quality of agreement was not found for the model predictions and measurements near the overload location (Site III). Although the trend is correct, not all measurement points are matched well.

Further measurements were performed at the final crack tip Sites IV and V. In Fig.13e-f, correct trend is seen between model values and FIB-DIC ring-core measurement points, but the magnitude varies. Finally, for the line extended beyond the crack tip reported in Fig.13g-h, good match was observed for both *xx* and *yy* components of stress, in that similar trends and satisfactory magnitude agreement were achieved. Particularly, the residual stress shown in Fig.13h can be compared to the outcomes of [11]. In fact, in this work the authors attempted the measurement of residual stress at the crack tip, by means of indentation technique. At the near crack tip, the residual stress trend turned out to be very close to that reported in the present paper. Likewise the FIB-DIC method, indentation provides information about the residual stress state at the free surface. Since also the gauge volume is in the same order of magnitude, qualitatively, the two results can be compared. Other techniques have been successfully adopted for stress measurement at the crack tip [6,7,9,34], but in those cases, an average value was evaluated along the entire sample thickness using Synchrotron-based Powder Diffraction (SPD). Even though the gauge volume was considerably

different from the one used in the present paper, the compressive residual stress region that we experienced was also found by measurement using SPD.

At this point it is worth noting that a range of various simplifications were adopted in the numerical model. For example, the discretisation of crack propagation steps may need refining in order to accurately reproduce the amount of residual stress left at the crack wake as the crack itself propagates. Also, although elastic anisotropy of single crystal aluminium is relatively low and can be considered negligible, plastic anisotropy induced by crystal slip may cause large variation in the effective yield stress according to the Schmid factor for slip. Furthermore, whilst in the overload region deformation is dominated by the single load application and unloading, elsewhere along the crack flanks the material experiences cyclic deformation that corresponds to a different hardening behaviour. Accurate description of the Bauschinger effect is likely to improve the accuracy of modelling. These considerations provide a means of understanding the discrepancy, and also give justification for further, more detailed analysis using crystal plasticity modelling.

Furthermore, the model used in the present analysis does not take into account the real crack path meandering that is significant at the fine scale. Small crack path deviation from the idealised straight line changes local stress conditions and in turn changes the resultant residual stress field. For instance, the map depicted in Fig.6b shows a localised area (indicated by the square in red) where intense plastic deformation is present. This corresponds to a steep change in the crack propagation direction.

It is important to note that experimental residual stress measurements were performed at the micron scale. As a consequence, intragranular stress values were obtained in most cases. In contrast, FEM simulation did not take into account the microstructure and stress variation within and between grains. Also, ad additional simplification is made assuming that the problem is two-dimensional while in reality the three-dimensionality effect might have its contribution. Finally, it is

also well known that the difference in deformation response between phases and their interaction has profound effect on the local residual stress evolution [35-37].

It is important to consider that all present outcomes are based on experiments performed using a single sample. Therefore, a variability of the results may be observed if exactly the same experiments are reproduced using a similar sample. This is due the quasi-random distribution of the material grain size, shape and orientation which may have a remarkable impact on local crack path shape and crack propagation rate.

5. Conclusion

The mechanisms involved in crack growth retardation after overload have been the subject of intense study for many decades. The principal aspects of the problem usually brought into consideration are plastic deformation, residual stress, and material property modification (hardening and damage). Identifying and separating the influence of each effect on the overall propagation rate is important for constructing reliable predictive models for the resulting deviation from steady state crack growth rate prescribed by the Paris law. In this study we focused our attention on two aspects of the problem, namely, plastic deformation (and in particular its consequence in terms of lattice distortion, that can be assessed using Electron BackScatter Diffraction), and residual stress that can be evaluated at the appropriate length scale using Focused Ion Beam and Digital Image Correlation (FIB-DIC) analysis. Plastic strain evaluation by EBSD revealed that areas of high deformation (lattice distortion) were found both along the crack flanks and at the overload site. Residual stress state around the crack is complex and arises due to the combination of the steady state plastically deformed layer developed along at the crack flank during fatigue crack propagation over many cycles, and also due to the much larger single overload plastic zone and the associated change in the

crack flank profile that leads to crack closure. High misorientation and plastic deformation (and hence residual stress) were in evidence in the area of overload (OL).

Of particular interest is the clear evidence that the overload caused complete arrest of the major crack and led to the nucleation of a new, deflected crack. By all appearances, this important phenomenon occurred immediately during and following the overload. If this scenario is to be accepted, then the apparent crack retardation occurs due to the combined influence of the crack driving force reduction due to deflection, and the effect of residual compressive stress caused by the formation of the large plastic zone ahead of the crack tip.

In order to substantiate further the arguments given above, FIB-DIC micro-ring-core method was employed to quantify the magnitude of micron-scale residual stresses found at locations of interest around the crack. The results were critically compared with the predictions of FE simulations for a homogenous, isotropic, simple hardening material model. The purpose of this comparison was to identify which aspects of the complex crack growth process could be captured correctly based on this fundamental model, and which require more refined simulation. The results open the avenues towards better understanding of the stress field generated by the overload and crack propagation. It can be noted that in general the expected trends were seen in almost the entire set of measurements, although for some locations the agreement was not found in terms of stress magnitudes. This mismatch may be imputed to several aspects not captured correctly in the numerical model, such as the influence of local cyclic hardening on the stress-strain curve, crack profile change due to local crack kinking, and local material anisotropy and inhomogeneity that were not included in the simulation. A more detailed model ought to be constructed that would take into account these aspects to describe faithfully the residual stress field.

Acknowledgements

AMK acknowledges funding received by MBLEM through EU FP7 project iSTRESS (604646).

References

[1] R.L. Carlson, G.A. Kardomateas and P.R. Bates. The effects of overloads in fatigue crack growth. International Journal of Fatigue 13 No. 6 (1991) pp 453-460

[2] K. Sadananda,A.K. Vasudevan, R.L. Holtz, E.U. Lee. Analysis of overload effects and related phenomena. International Journal of Fatigue 21 (1999) S233–S246

[3] F.S. Silva. Fatigue crack propagation after overloading and underloading at negative stress ratios. International Journal of Fatigue 29 (2007) 1757–1771

[4] L. Lawson, E.Y. Chen, M. Meshii. Near-threshold fatigue: a review. International Journal of Fatigue 21 (1999) S15–S34

[5] F.V. Antunes, T. Sousa, R. Branco, L. Correia. Effect of crack closure on non-linear crack tip parameters. International Journal of Fatigue 71 (2015) 53–63

[6] A. Steuwer, M. Rahman, A. Shterenlikht, M.E. Fitzpatrick, L. Edwards, P.J. Withers. The evolution of crack-tip stresses during a fatigue overload event. Acta Materialia 58 (2010) 4039–4052

[7] P. Lopez-Crespo, A. Steuwer, T. Buslaps, Y.H. Tai, A. Lopez-Moreno, J.R. Yates, P.J. Withers. Measuring overload effects during fatigue crack growth in bainitic steel by synchrotron X-ray diffraction. International Journal of Fatigue 71 (2015) 11–16

[8] A.M. Korsunsky, M. R. Daymond, Karen E. Wells. The Development of Strain Anisotropy During Plastic Deformation of an Aluminium Polycrystal.

[9] A.M. Korsunsky, X. Song, J. Belnoue, T. Jun, F. Hofmann, P. F.P. De Matos, D. Nowell, D. Dini, O. A. Blanco, M. J. Walsh. Crack tip deformation fields and fatigue crack growth rates in Ti–6Al–4V. International Journal of Fatigue 31 (2009) 1771–1779

[10] M.N. James, C.J. Christopher, Y. Lu, E.A. Patterson. Local crack plasticity and its influences on the global elastic stress field. International Journal of Fatigue 46 (2013) 4–15

[11] L. Xiao, D. Ye, C. Chen, J. Liu, L. Zhang. Instrumented indentation measurements of residual stresses around a crack tip under single tensile overloads. International Journal of Mechanical Sciences 78 (2014) 44–51

[12] J. Haigen, Y. Zhimin, J. Feng, L. Xue. EBSD Analysis of Fatigue Crack Growth of 2124 Aluminum Alloy for Aviation. Rare Metal Materials and Engineering, 2014, 43(6): 1332-1336

[13] H. Jian, F. Jiang, L. Wei, X. Zheng, K. Wen. Crystallographic mechanism for crack propagation in the T7451 Al–Zn–Mg–Cu alloy. Materials Science and Engineering A 527 (2010) 5879–5882

[14] S. I. Wright, M.M. Nowell, D. P. Field. A review of Strain Analysis Using Electron Backscatter Diffraction. Microsc. Microanal. 17, 316-329, 2011. DOI: 10.1017/S1431927611000055.

[15] T.B. Britton, A.J. Wilkinson. High resolution electron backscatter diffraction measurements of elastic strain variations in the presence of larger lattice rotations. Ultramicroscopy 114 (2012) 82–95.

[16] A. J. Wilkinson, T. B. Britton. Strains, planes, and EBSD in materials science. Materials Today. September 2012. Vol 15. Number 9

[17] A.M. Korsunsky, M. Sebastiani, E. Bemporad. Focused ion beam ring drilling for residual stress evaluation. Material Letters 63, 1961-1963, (2009).

[18] E. Bemporad, M. Brisotto, L.E. Depero, M. Gelfi, A.M. Korsunsky, A.J.G. Lunt, M. Sebastiani. A critical comparison between XRD and FIB residual stress measurement techniques in thin films. Thin Solid Films 572 (2014) 224–231

[19] E. Salvati, T. Sui, A. J.G. Lunt, A. M. Korsunsky. The effect of eigenstrain induced by ion beam damage on the apparent strain relief in FIB-DIC residual stress evaluation. Materials & Design, Volume 92, 15 February 2016, Pages 649-658

[20] X. Song, K.B. Yeap, J. Zhu, J. Belnoue, M. Sebastiani, E. Bemporad, K.Y. Zeng, A. M. Korsunsky. Residual stress measurement in thin films using the semidestructive ring-core drilling method using Focused Ion Beam. Proc. Eng. 10 (2011) 2190–2195

[21] Y. Murakami. Stress Intensity Factors Handbook Volume 2, Pergamon Press (1987)

[22] Irwin, G. R. (1958). In "Handbuch der Physik," Vol. 6, pp. 551-590. Springer, Berlin

[23] J. Zuidema, P. J. M. Menses, R. A. H. Edwards. Environmental Dependence Of Fatigue Crack Growth Retardation Following A Single Overload In 2024-Al Alloy. Engineering Fracture Mechanics Vol. 26, No. 6, pp. 921-935, 1987. Printed m Great Britain.

[24] Z. Ting, B, Rui, F. Binjun. Load effects on macroscopic scale fatigue crack growth path in 2324-T39

aluminium alloy thin plates. International Journal of Fatigue 58 (2014) 193–201

[25] K.T. Venkateswara Rao, R.O. Ritchie. Mechanisms for the retardation of fatigue cracks following single tensile overloads: behavior in aluminum-lithium alloys. Acta Metallurgica Volume 36, Issue 10, October 1988, Pages 2849–2862

[26] A.M. Korsunsky , M.R. Daymond and K.E. James.The correlation between plastic strain and anisotropy strain in aluminium alloy polycrystals. (2012) Materials Science And Engineering A-Structural Materials Properties Microstructure And Processing. Volume: 334 Issue: 1-2 Pages: 41-48 Article Number: PII S0921-5093(01)01780-4

[27] X. Song, F. Hoffman and A.M. Korsunsky. Dislocation-based plasticity model and micro-beam Laue diffraction analysis of polycrystalline Ni foil: A forward prediction. (2010) Philosophical Magazine Volume: 90 Issue: 30 Pages: 3999-4011 Article Number: Pii 925183310.

[28] F. Hofmann, D. Nguyen-Manh, M.R. Gilbert, C.E. Beck, J.K. Eliason, A.A. Maznev, W. Liu. D.E.J. Armstrong, K.A. Nelson and S.L. Dudarev. Lattice swelling and modulus change in a helium-implanted tungsten alloy: X-ray micro-diffraction, surface acoustic wave measurements, and multiscale modelling. Acta Materialia 89 (2015) 352–363

[29] L. Brewer, M. Othon, and T. Angeliu. Characterizing local strain variations around crack tips using EBSD mapping. *Application note*. Web site: http://www.oxford-instruments.com/getmedia/2cf71e40-9a0d-4f49-9113-69475a4c84fb/Characterising-local-strain-variations-around-crack-tips-using-EBSD-mapping (2016)

[30] J. P. Belnoue, T.-S. Jun, F. Hofmann, B. Abbey, A. M. Korsunsky. Evaluation of the overload effect on fatigue crack growth with the help of synchrotron XRD strain mapping. Engineering Fracture Mechanics 77 (**2010**) 3216–3226

[31] C. Eberl. Digital Image Correlation and Tracking (Software). Web site (Nov.2015): http://www.mathworks.com/matlabcentral/fileexchange/12413-digital-image-correlation-and-tracking

[32] E. Salvati, M. Benedetti, T. Sui and A. M. Korsunsky. Residual Stress Measurement on Shot Peened Samples Using FIB-DIC. Conference proc. SEM 2015, Costa Mesa - California; 06/2015

[33] E. Salvati, T. Sui and A.M. Korsunsky. Uncertainty Quantification of Residual Stress Evaluation by the FIB-DIC Ring-Core Method due to Elastic Anisotropy Effects. International Journal of Solids and Structures. In Press, Corrected proof. doi:10.1016/j.ijsolstr.2016.02.031

[34] H. Wang, F.G. Buchholz, H.A. Richard, S. Jagg, B. Scholtes. Numerical and experimental analysis of residual stresses for fatigue crack growth. Computational Materials Science 16 (1999) 104-112

[35] Y. Onuki, S. Fujieda, R. Ukai, S. Sato, M. Sato , K. Kajiwara, S. Suzuki. Local stress development in polycrystalline Fe-17mol%Ga alloy under tensile loading e In situ measurement using synchrotron X-ray micro-beam. Journal of Alloys and Compounds 653 (2015) 195e201

[36] C.R. Chen, S.X. Li. Distribution of stresses and elastic strain energy in an ideal multicrystal model. Materials Science and Engineering A257 (1998) 312–321.

[37] F. Hofmann, X. Song, B. Abbey, T. S. Jun and A.M. Korsunsky. High-energy transmission Laue micro-beam X-ray diffraction: a probe for intra-granular lattice orientation and elastic strain in thicker samples. J. Synchrotron Rad. (2012). 19, 307–318.

Captions

Figure 1: a) Sample geometry (all dimensions are given in mm). b) The loading history.

Figure 2. Fatigue Crack Growth curve

Figure 3: SEM images of the crack obtained from an unpolished surface a) before the overload application, at Fmax=1.25kN (B), and b) after the application of the overload, at Fmin=0.125kN (D').

Figure 4: SEM images of the crack tip obtained from the unpolished surface at various instants in the crack growth history: a) before OL at Fmin=0.125kN (B'), b) at OL, at FOL=1.875kN (OL), c) after OL, at Fmin=0.125kN (C'), and d) after OL at Fmin=0.125kN (D').

Figure 5: A superposition map of grain orientation (colour derived from the inverse pole figure for the Rolling Direction shown in the inset) on the grey scale Kikuchi band contrast map for the crack over the length of 1.75mm on the polished surface of sample cross-section. The location of OL application is indicated by the yellow circle.

Figure 6: Inverse Pole Figures (with respect to the rolling direction) obtained for the three principal phases within the material. The colour bar is given in terms of the multiple of uniform density (m.u.d.) a) Al. b) Al Mn3 C. c) Al0.3 Cu7.01 Fe1.7 Mg0.2

Figure 7: a) Orientation map obtained from the polished surface of sample cross-section around the crack grown beyond the overload application. The overload site is indicated by the letter "A", and the final crack tip by the letter "B". b) Contour map of deformation intensity, as derived from EBSD misorientation evaluation.

Fig.8. FIB-DIC milling positions across the crack path. The dashed white lines indicate the spatially resolved line measurements while the white dots denote the single point measurements.

Fig.9. a) Illustration of the progress of the milling procedure (measurements in μm) b) Strain relief curve fitting example. *D* is the pillar diameter and *h* is the trench depth.

Fig.10. Discretised 2D model, mesh refinement details at regions of interest

Fig.11. Residual stress obtained by FIB-DIC along the crack flanks extension (Site I).

Fig.12. Stress yy component contour plots. a) At the overload (OL). b) At B'' and c) At D''. The solid line indicates the formed crack. d) Magnified region of interest from Fig. 8.

Fig.13. Residual stress comparison. FIB-DIC vs. FE simulation. a) σ_yy Site II, b) σ_xx Site II, c) σ_yy Site III, d) σ_xx Site III, e) σ_yy Site IV, f) σ_xx Site IV, g) σ_yy Site V, h) σ_xx Site V

Figures

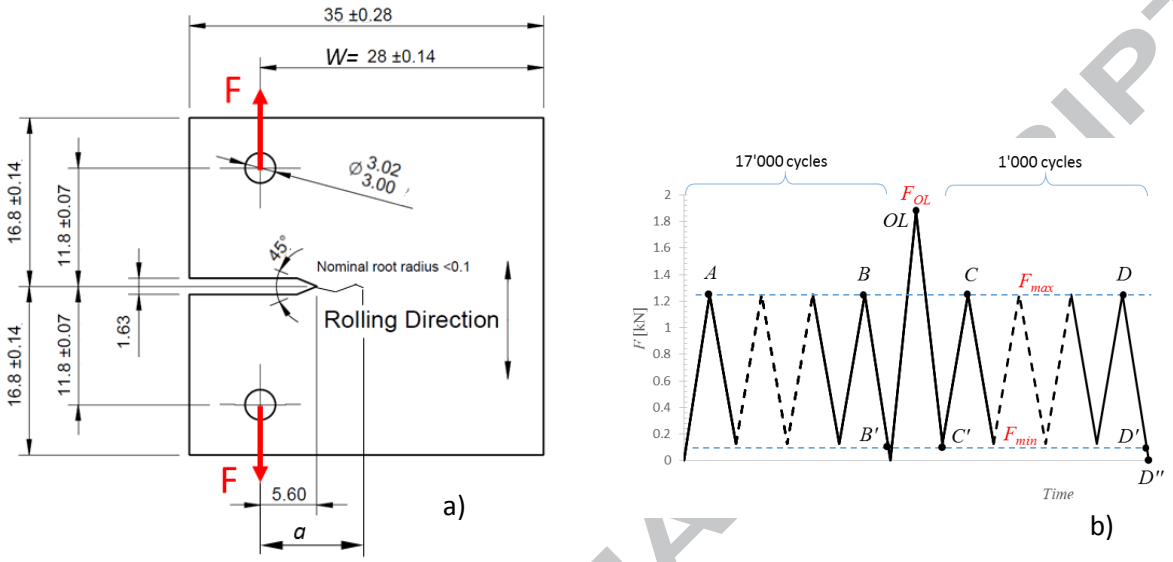

Figure 1: a) Sample geometry (all dimensions are given in mm). b) The loading history.

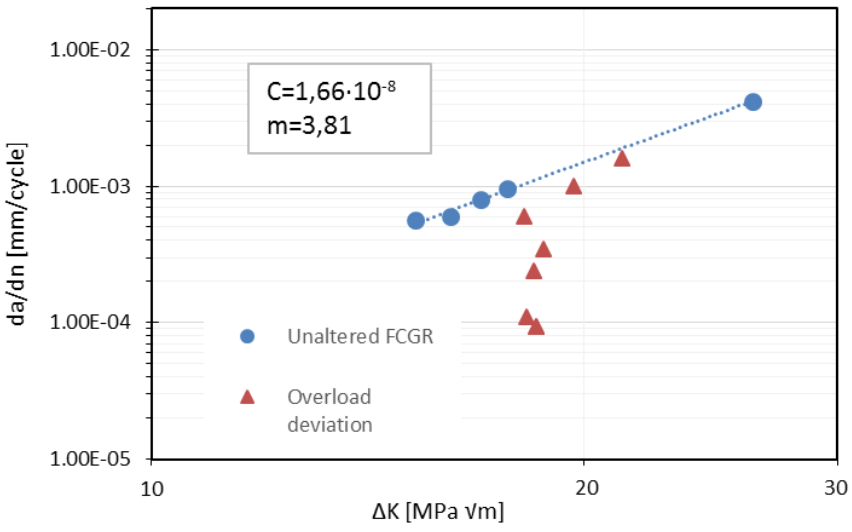

Figure 2. Fatigue Crack Growth curve

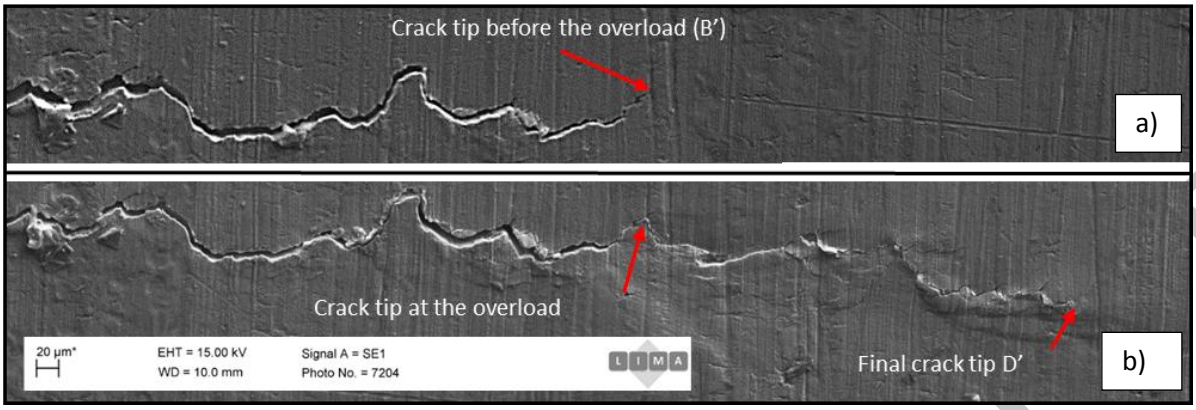

Figure 3: SEM images of the crack obtained from an unpolished surface a) before the overload application, at F_{max}=*1.25kN* (B), and b) after the application of the overload, at F_{min}=*0.125kN* (D').

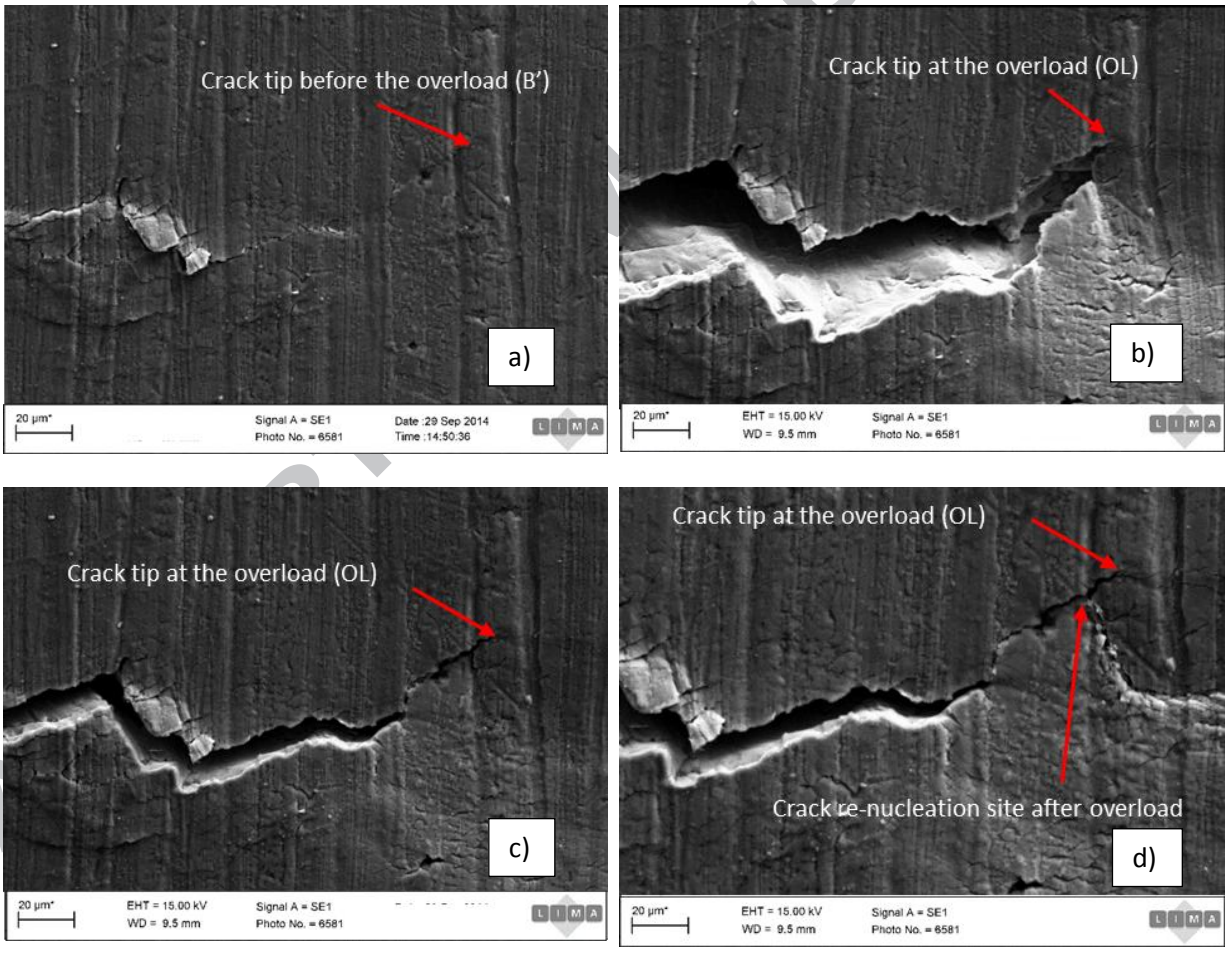

Figure 4: SEM images of the crack tip obtained from the unpolished surface at various instants in the crack growth history: a) before OL at F_{min}=*0.125kN* (B'), b) at OL, at F_{OL}=*1.875kN* (OL), c) after OL, at F_{min}=*0.125kN* (C'), and d) after OL at F_{min}=*0.125kN* (D').

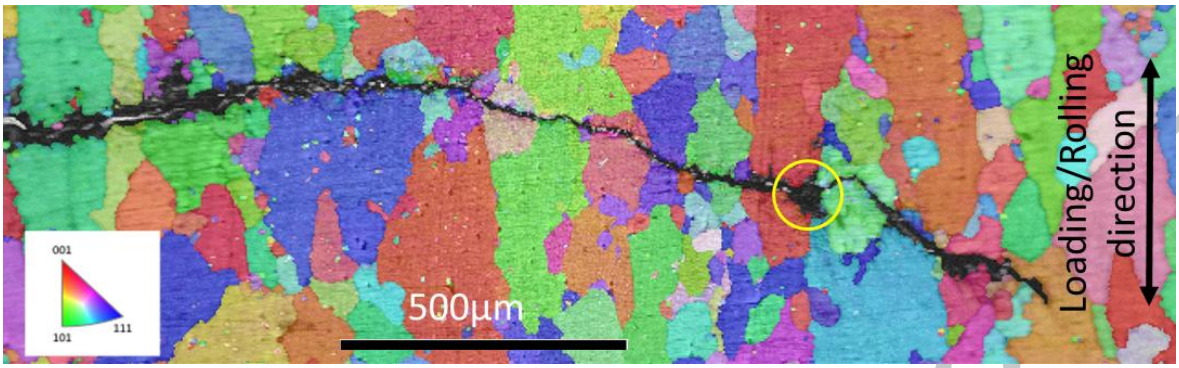

Figure 5: A superposition map of grain orientation (colour derived from the inverse pole figure for the Rolling Direction shown in the inset) on the grey scale Kikuchi band contrast map for the crack over the length of 1.75mm on the polished surface of sample cross-section. The location of OL application is indicated by the yellow circle.

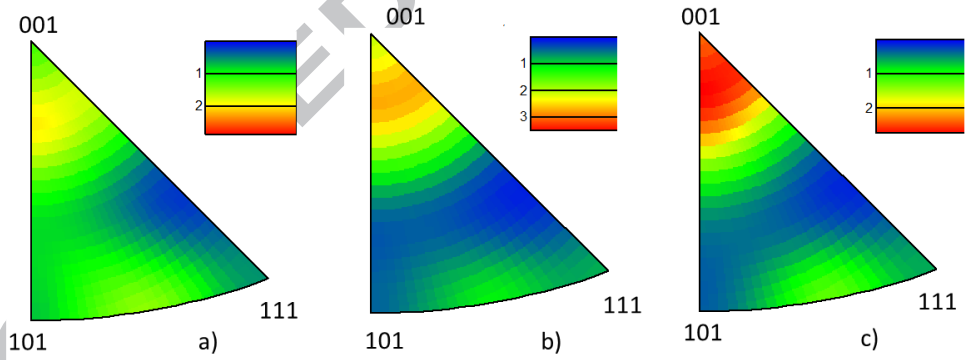

Figure 6: Inverse Pole Figures (with respect to the rolling direction) obtained for the three principal phases within the material. The colour bar is given in terms of the multiple of uniform density (m.u.d.) a) Al. b) Al Mn_3 C. c) $Al_{0.3}Cu_{7.01}Fe_{1.7}Mg_{0.2}$

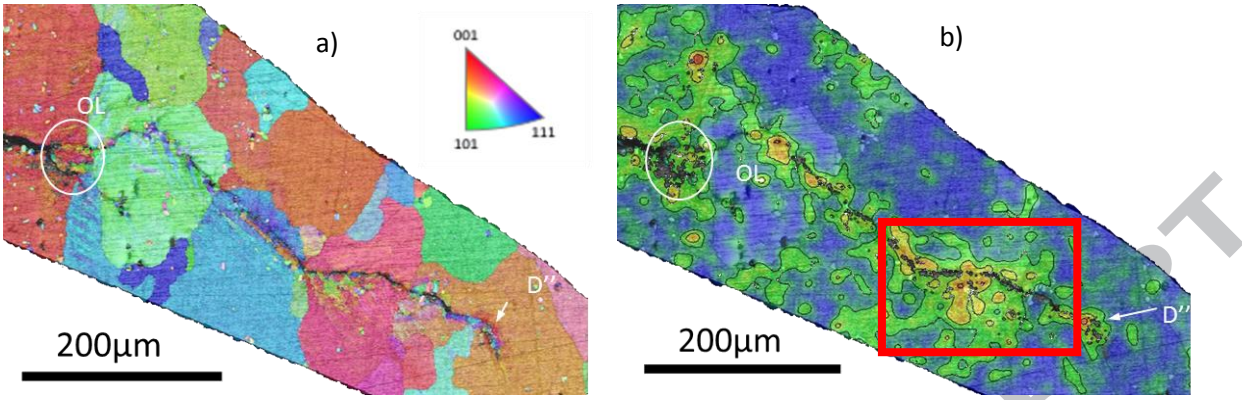

Figure 7: a) Orientation map obtained from the polished surface of sample cross-section around the crack grown beyond the overload application. The overload site is indicated by the letters OL, and the final crack tip by the letter D''. b) Contour map of deformation intensity, as derived from EBSD misorientation evaluation.

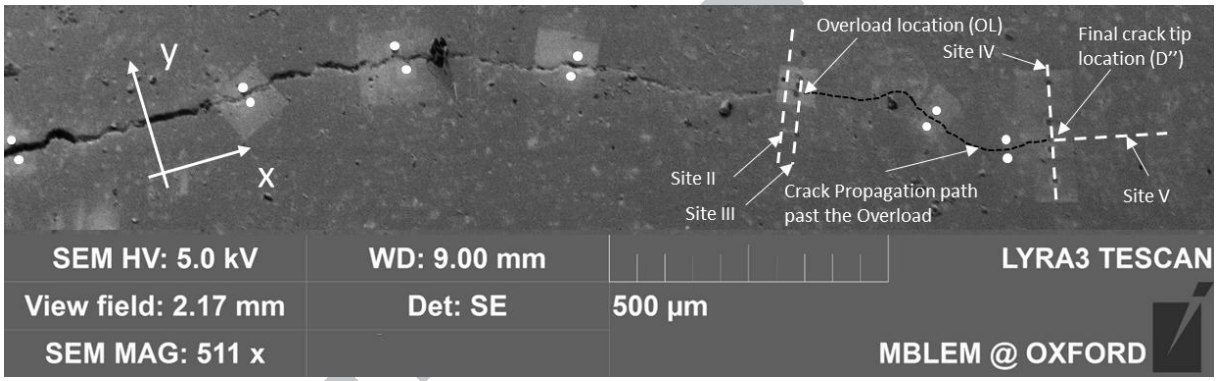

Fig.8. FIB-DIC milling positions across the crack path. The dashed white lines indicate the spatially resolved line measurements while the white dots denote the single point measurements.

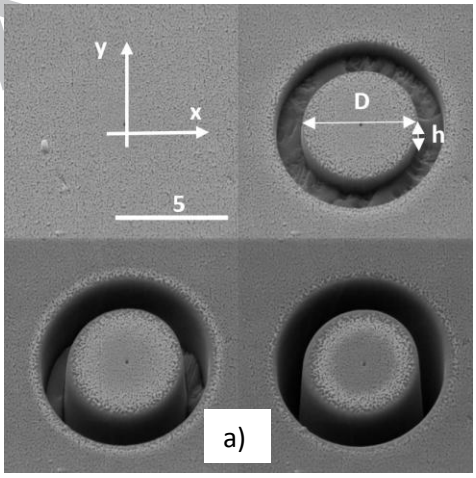

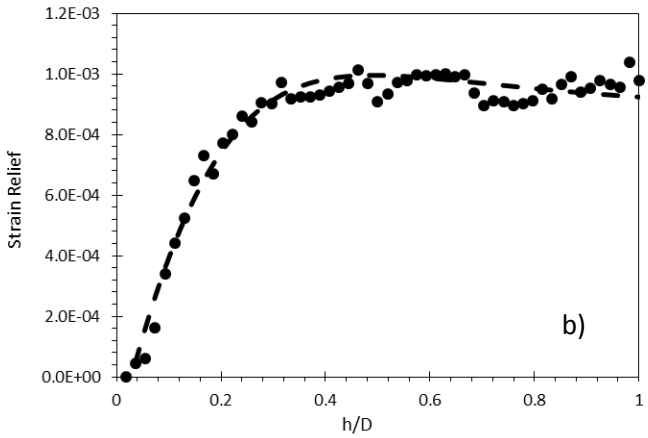

Fig.9. a) Illustration of the progress of the milling procedure (measurements in μm) b) Strain relief curve fitting example. *D* is the pillar diameter and *h* is the trench depth.

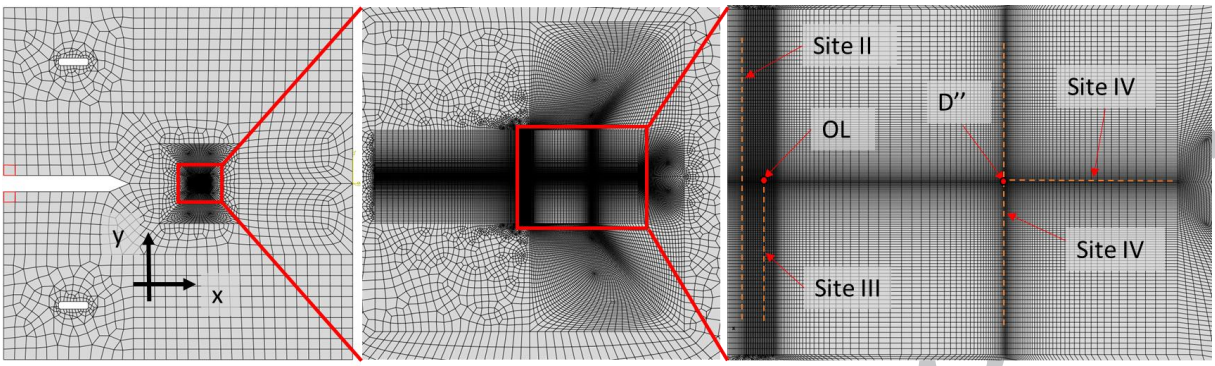

Fig.10. Discretised 2D model, mesh refinement details at regions of interest

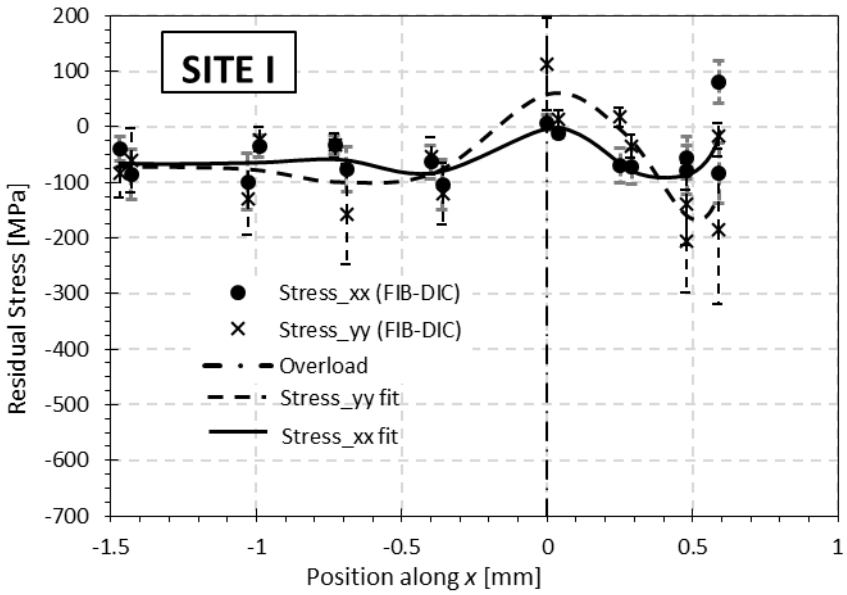

Fig.11. Residual stress obtained by FIB-DIC along the crack flanks extension (Site I).

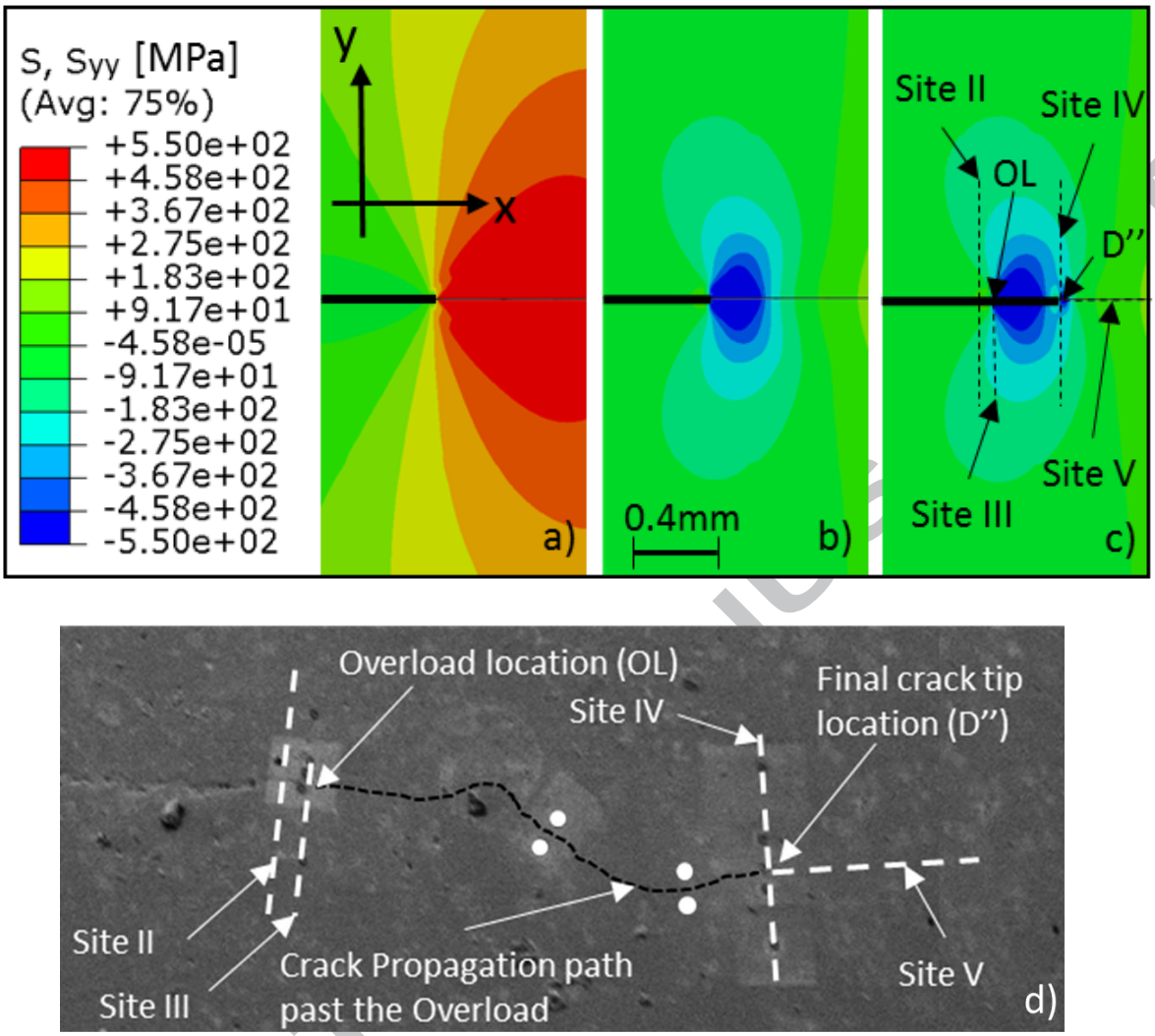

Fig.12. Stress *yy* component contour plots. a) At the overload (OL). b) At B'' and c) At D''. The solid line indicates the formed crack. d) Magnified region of interest from Fig. 8.

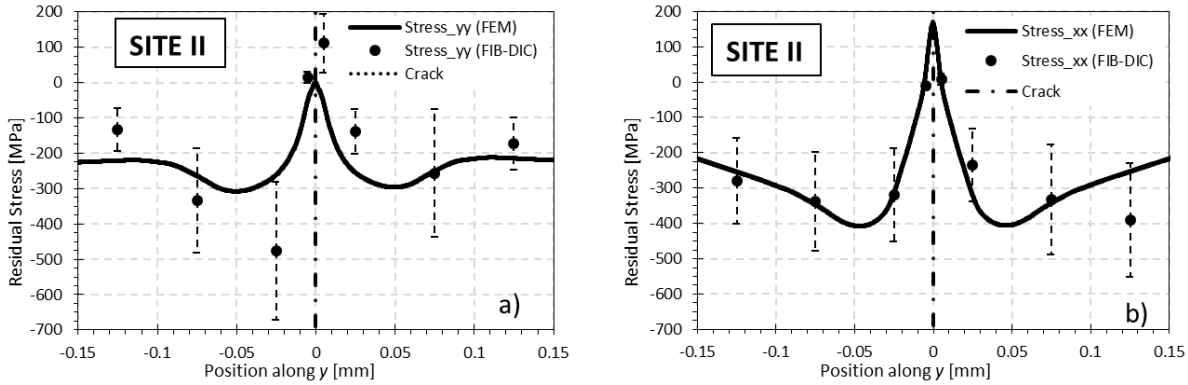

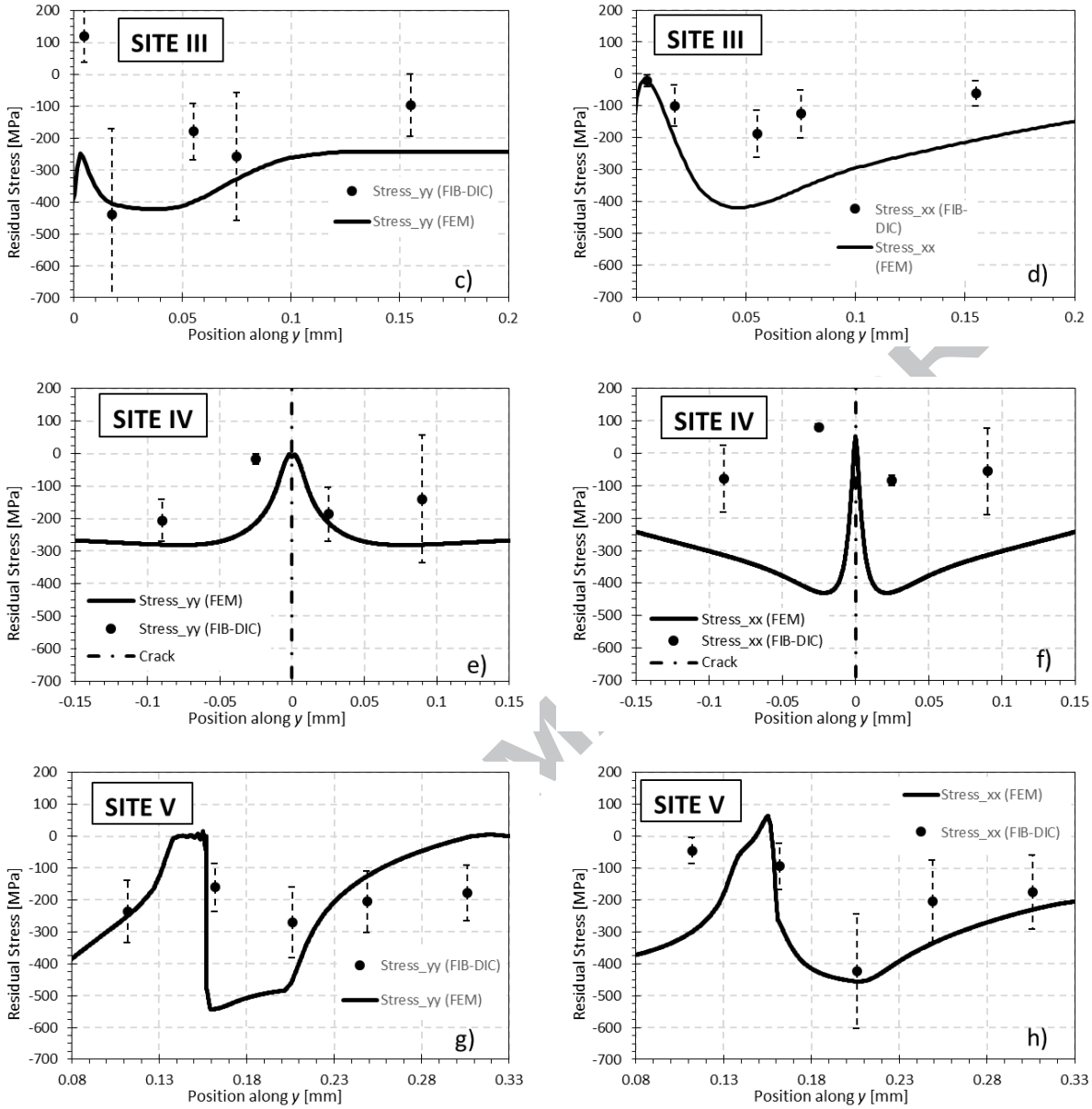

Fig.13. Residual stress comparison. FIB-DIC vs. FE simulation at the propagation stage D''. a) σ_{yy} Site II, b) σ_{xx} Site II, c) σ_{yy} Site III, d) σ_{xx} Site III, e) σ_{yy} Site IV, f) σ_{xx} Site IV, g) σ_{yy} Site V, h) σ_{xx} Site V

Nomenclautre

K_I mode I stress intensity factor

ΔK stress intensity factor range

F applied force to the specimen

ΔF cyclic force range

F_{min} minimum force applied to the specimen

F_{max} maximum force applied to the specimen

F_{OL} Overload force applied to the specimen

b specimen thickness

W Specimen width

a crack length

da/dn fatigue crack growth rate

C Paris' law intercept coefficient

m Paris law slope coefficient

E Young's modulus

ν Poisson's ratio

σ_{xx} Stress (xx component)

σ_{yy} Stress (yy component)

ε_{xx} Strain (xx component)

ε_{yy} Strain (yy component)

n Hardening exponent

K Strength coefficient